

## Supporting Information

# Interfaced Metal Heterodimers in the Quantum Size Regime

*Yugang Sun,<sup>\*†</sup> Jonathan J. Foley,<sup>†</sup> Sheng Peng,<sup>†</sup> Zheng Li, and Stephen K. Gray<sup>\*</sup>*

*Center for Nanoscale Materials, Argonne National Laboratory, 9700 South Cass Avenue,  
Argonne, Illinois 60439, United States*

E-mail: [ygsun@anl.gov](mailto:ygsun@anl.gov) (YS) and [gray@anl.gov](mailto:gray@anl.gov) (SKG)

### **Contents:**

1. Supplementary Experimental Information and Results
2. Theoretical Model
  - A. Heterodimer Dielectric Constant
  - B. Electrodynamics Computational Details
  - C. Electronic Structure Computational Details

# 1. Supplementary Experimental Information and Results

## Synthesis of interfaced Au-Ag heterodimers

1. *Synthesis of Au nanoparticles a diameter of 5.9 nm*: In a typical synthesis, 0.094 g of hydrogen tetrachloroaurate (III) hydrate ( $\text{HAuCl}_4 \cdot 3\text{H}_2\text{O}$ , Strem Chemicals) was first dissolved in 5 mL of 1,2,3,4-tetrahydronaphthalene (tetralin, 95–98%, Acros Organics) and 6 mL of oleylamine (OAm with C18 content of 80-90%, Acros Organics), resulting in an organic precursor solution. The atmosphere above the solution was purged with  $\text{N}_2$  flow for 10 min. To this solution was added a reducing solution containing 49 mg *tert*-butylamine-borane complex (TBAB, 97%, Sigma-Aldrich) dissolved in 0.6 mL of OAm and 0.5 mL of tetralin through a quick injection. The reduction was instantaneously initiated and the solution changed to a deep purple color within 5 s. The reaction solution was incubated for 10 h under the  $\text{N}_2$  blanket cover. The whole synthesis process was performed at room temperature (i.e., 22 °C). The synthesized Au nanoparticles were then precipitated by adding acetone to the reaction solution followed by centrifugation at 8500 rpm for 8 min. The settled Au nanoparticles were washed with acetone and redispersed in hexane for future use and characterization.

2. *Coating of the Au nanoparticles with a very thin layer of iron oxide*: 12 mg of the synthesized Au nanoparticles that were obtained after evaporation of hexane were redispersed in 10 mL of 1-octadecene (ODE, 90%, Sigma-Aldrich) and 0.1 mL of OAm that stabilized the Au nanoparticles. The solution was prepared in a 3-neck flask that was connected to the standard Schlenk line. The whole system was purged with  $\text{N}_2$  flow for 10 min at room temperature. With the protection of the  $\text{N}_2$  flow, the dispersion of the Au nanoparticles was then heated to 120 °C and maintained at this temperature for 5 min. The temperature of the dispersion was further increased to 150 °C under the  $\text{N}_2$  blanket cover followed by injection of 0.05 mL iron pentacarbonyl ( $\text{Fe}(\text{CO})_5$ , Sigma-Aldrich). The reaction was maintained at 150 °C for 5 min and the reaction solution was quickly cooled to room temperature with hexane spray.

3. *Epitaxial overgrowth of Ag on the iron oxide-passivated Au nanoparticles*: In a typical synthesis, 10 mg of partially passivated Au nanoparticles were redispersed in 12 mL of ODE and 1 mL of OAm in a 3-neck flask connected to a standard Schlenk line. The whole system was purged with  $\text{N}_2$  flow for 10 min at room temperature. With the protection of the  $\text{N}_2$  flow, the

dispersion of the Au nanoparticles was then heated to 120 °C and maintained at this temperature for 5 min. The temperature of the dispersion was further increased to 180 °C under the N<sub>2</sub> blanket cover followed by injection of 2 mL OAm solution of AgNO<sub>3</sub> (0.03 M, Sigma-Aldrich). Aliquots (of 0.4 mL) were taken from the reaction solution at different times and were quickly added to 1.5 mL of hexane to cool the products. The resulting dispersions were used to measure their optical absorption spectra for quantitatively comparison.

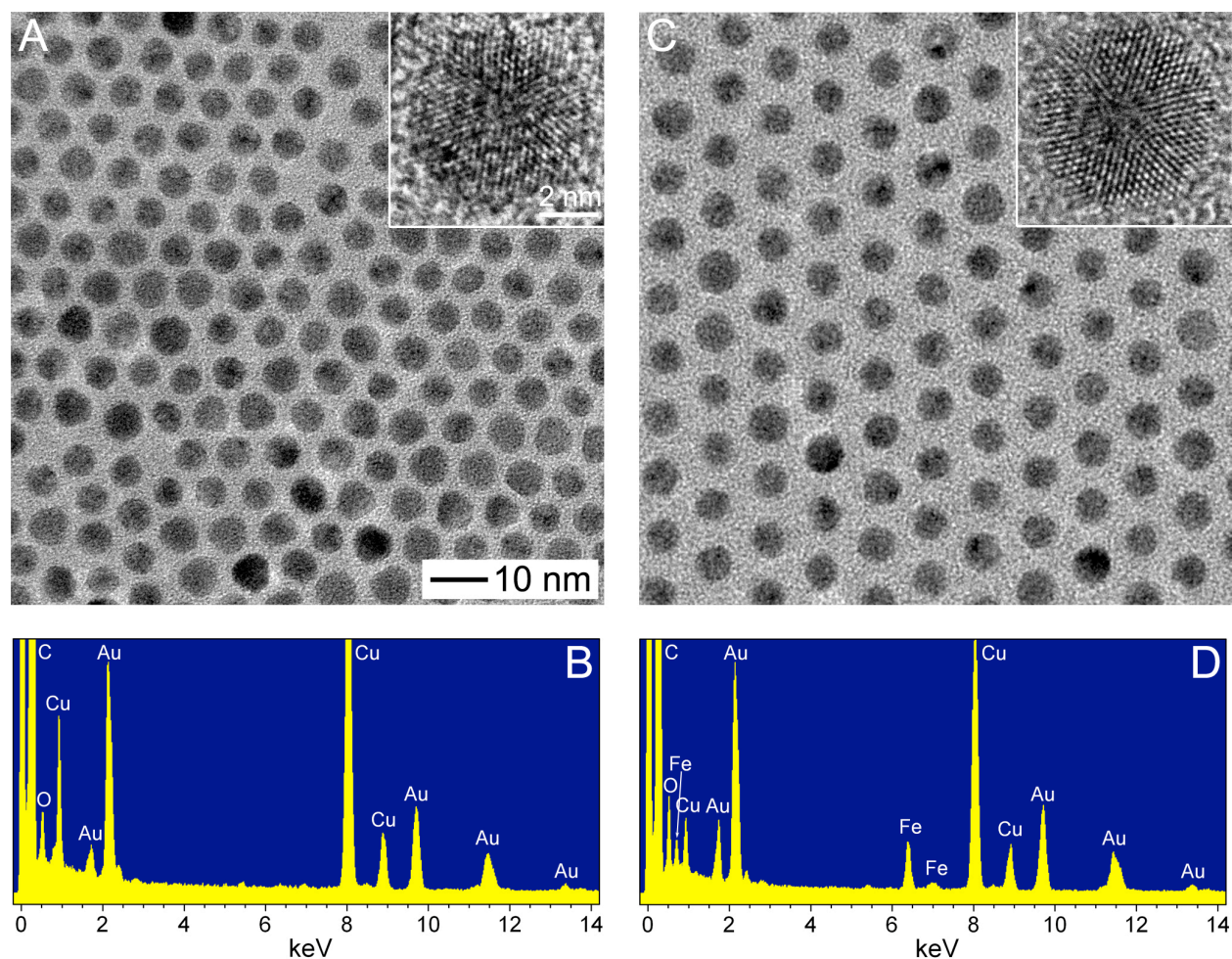
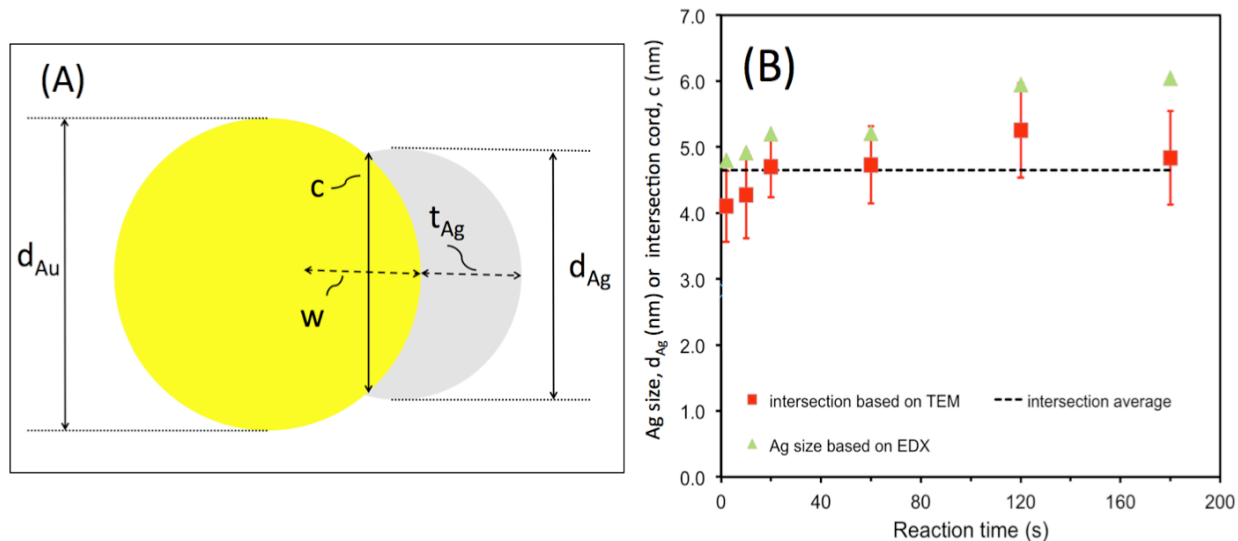


**Figure S1.** (A, C) TEM images and (B, D) EDS analysis of Au nanoparticles (A, B) before and (C, D) after their surfaces partially passivated with iron oxide. The HRTEM images shown as insets in (A, C) indicate that the crystalline structure of the Au nanoparticles remains the same after the modification with iron oxide. The signals of Au and Fe corresponding to the nanoparticles while the signals of Au and C originate from the TEM grids.



(C)

Reaction Time (s)	Au Diameter, $d_{Au}$ (nm)	Ag Diameter, $d_{Ag}$ (nm)	Cord of Intersection, $c$ (nm)	Overlap, $w$ (nm)	Maximum Ag Thickness, $t_{Ag}$ (nm)
0	5.90	0.00	--	--	0.0
2	5.90	4.80	4.60	2.82	1.98
10	5.90	4.92	4.60	2.70	2.22
20	5.90	5.20	4.60	2.49	2.71
120	5.90	5.94	4.60	2.19	3.75
180	5.90	6.04	4.60	2.16	3.88

**Figure S2.** (A) Schematic diagram highlighting the geometry of a model Au-Ag heterodimer: a Au sphere with a Ag nanodomain corresponding to the non-overlapping portion of a sphere displaced from the Au one. (B, C) Relevant dimensional parameters in the model deduced from the EDX spectra and TEM images of the products formed at various reaction times. The Au and Ag diameters,  $d_{Au}$  and  $d_{Ag}$ , and the cord of intersection,  $c$ , represent the quantities directly measured; the overlap of the spheres,  $w$ , and the maximum Ag nanodomain thickness,  $t_{Ag}$ , are obtained from these quantities with elementary geometry. The center-to-center separation of the spheres involved in the model is  $(d_{Au}+d_{Ag})/2 - w$ . The intersection was assumed to be constant as during the growth of the Ag domains.

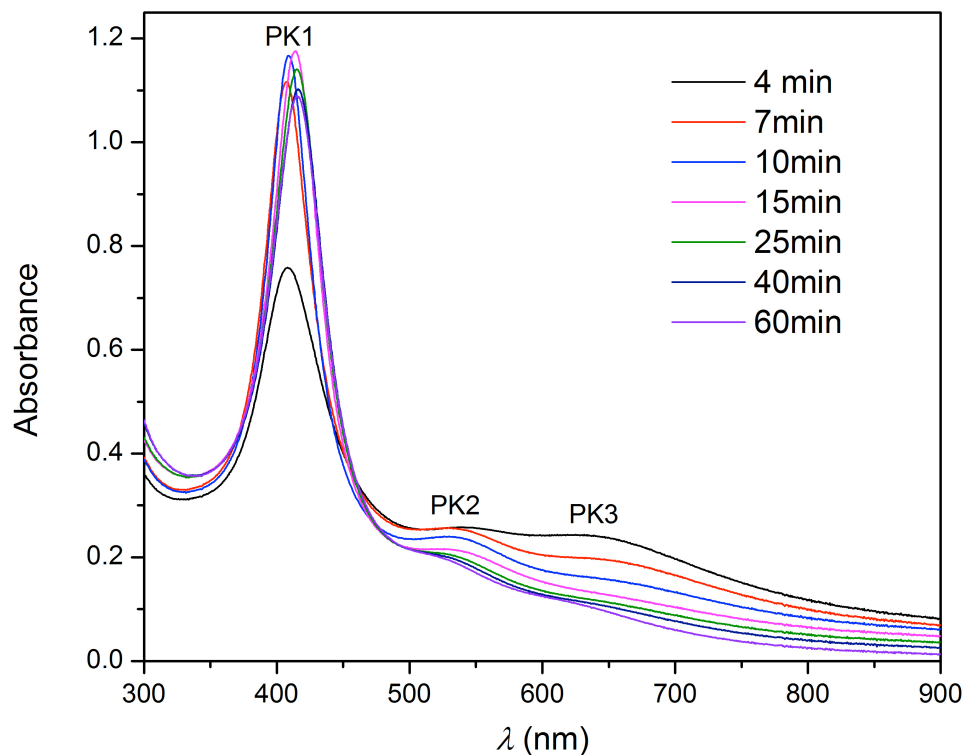


**Figure S3.** Absorption spectra of the products formed after the epitaxial overgrowth of Ag on the partially passivated Au nanoparticles shown in Figure 1A for different times longer than 4 minutes. The nanoparticles were dispersed in hexane for spectral characterization. The intensities of the spectra were normalized against the concentration of the Au nanoparticles that was maintained constant during the synthesis.

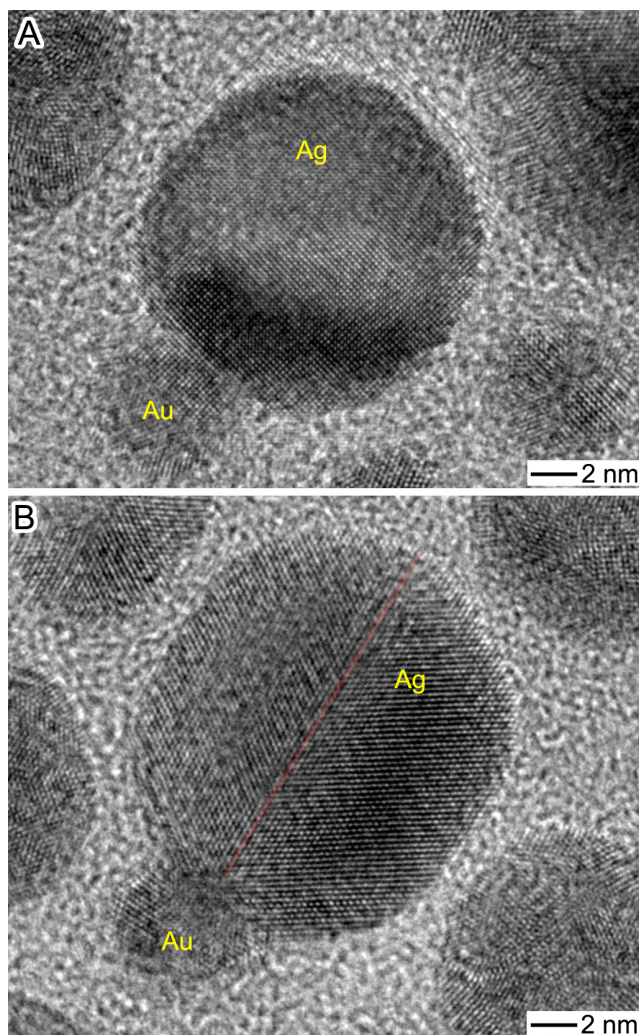


**Figure S4.** HRTEM images of individual interfaced Au-Ag dimers with Ag domains larger than the Au nanoparticles. The images clearly show the epitaxial relationship between the Au lattice and the Ag lattice at the Au/Ag interfaces. The red line in (B) highlights the existence of a twin plane.

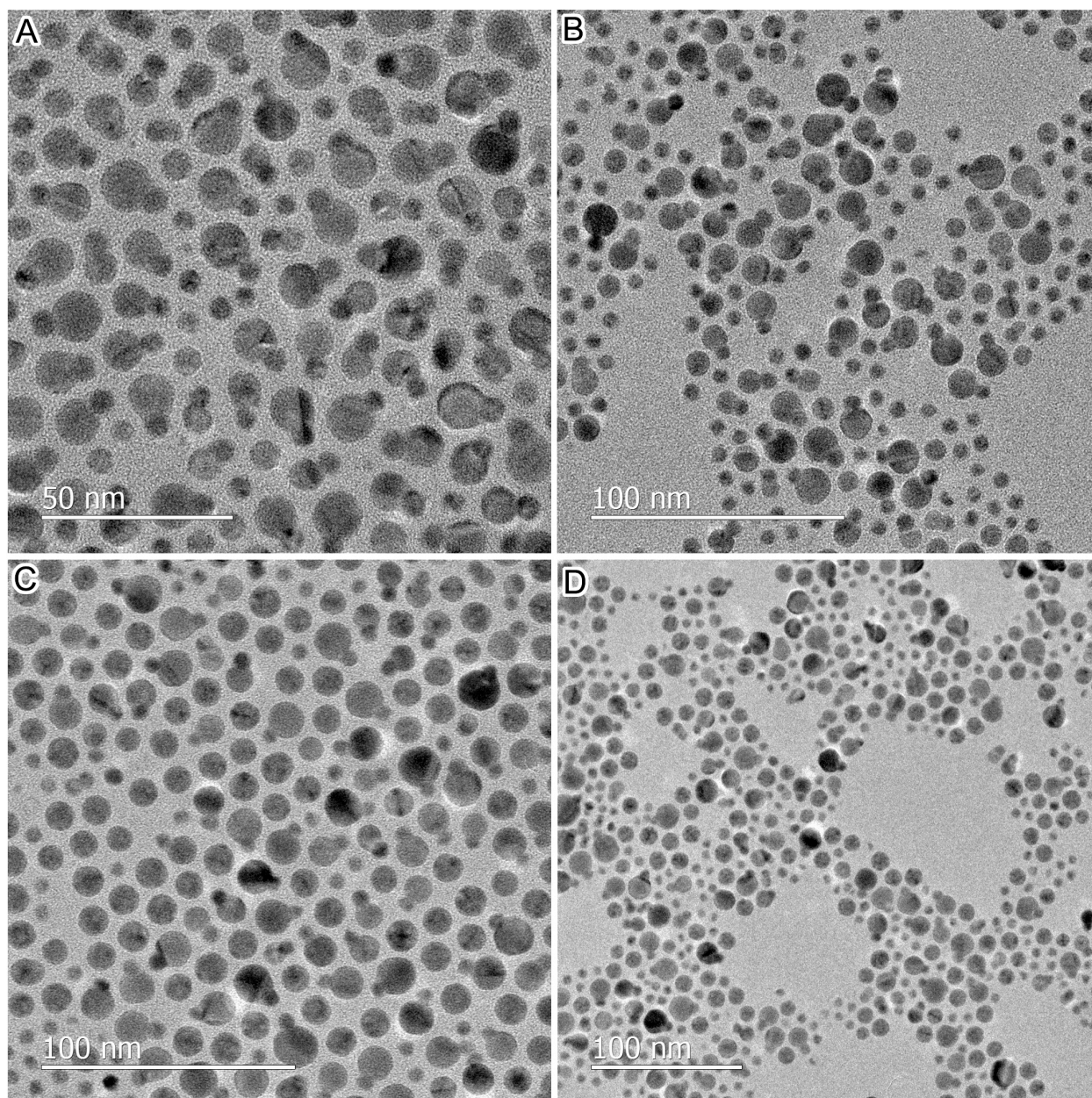


**Figure S5.** TEM images of the products formed after the epitaxial overgrowth of Ag on the partially passivated Au nanoparticles shown in Figure 1A for different times: (A) 7 min, (B) 15 min, (C) 40 min, and (D) 60 min.

## 2. Theoretical Model

### A. Heterodimer Dielectric Constant

For a given frequency or wavelength, the classical electrodynamics (DDA) calculations require specification of the dielectric constant at each point in space. For points that lie within the metal heterodimer structure, this (complex-valued) dielectric constant is denoted as  $\epsilon_X(\omega)$ , with  $X = \text{Au}$  or  $\text{Ag}$  as appropriate. In order to properly describe the experimental results,  $\epsilon_X(\omega)$  is size-corrected in a manner to account for the increased electron scattering within the heterodimer, including scattering at interfaces such as the Au/Ag interface, and chemical interactions of the outermost heterodimer layer with surfactant molecules as described below.

First we note that the bulk dielectric constant for metal  $X$ , which in practice we take from the empirical data of Johnson and Christy,<sup>1</sup> may be decomposed as

$$\epsilon_X^{\text{bulk}}(\omega) = \epsilon_X^{\text{intra},0}(\omega) + \epsilon_X^{\text{inter}}(\omega), \quad (\text{S1})$$

where the bulk intraband contribution,  $\epsilon_X^{\text{intra},0}(\omega)$ , is taken to be a Drude-model fit to the low-frequency or long-wavelength limiting values of  $\epsilon_X^{\text{bulk}}(\omega)$ ,

$$\epsilon_X^{\text{intra},0}(\omega) = \epsilon_X^\infty + \frac{(\omega_X^0)^2}{\omega^2 + i\omega\gamma_X^0}. \quad (\text{S2})$$

Note that once  $\epsilon_X^{\text{intra},0}(\omega)$  is determined, the interband contribution,  $\epsilon_X^{\text{inter}}(\omega)$ , is then simply defined to be  $\epsilon_X^{\text{bulk}}(\omega) - \epsilon_X^{\text{intra},0}(\omega)$ .

The size-corrected metal dielectric constant,  $\epsilon_X(\omega)$ , is taken to be

$$\epsilon_X(\omega) = \epsilon_X^{\text{intra}}(\omega) + \epsilon_X^{\text{inter}}(\omega), \quad (\text{S3})$$

where the size-dependence arises solely from the intraband term,  $\epsilon_X^{\text{intra}}(\omega)$ , which, like its bulk counterpart Eq. (S2), is given by a Drude model, but with some parameters different from the bulk case,

$$\epsilon_X^{\text{intra}}(\omega) = \epsilon_X^\infty + \frac{\omega_X^2}{\omega^2 + i\omega\gamma_X}. \quad (\text{S4})$$

Within each metal component of the heterodimer we take  $\omega_X$  to be the appropriate metal's bulk value,  $\omega_X^0$ , from Eq. (S2). However, within the 0.25 nm outer shell (i.e., one atomic layer) of the

heterodimer, due to the chemical interactions with the surfactant, we take  $\omega_X = g_X \omega_X^0$ . Since the plasma frequency is proportional to the square root of the carrier density, and thus also to the square root of the AC conductivity, this corresponds to assuming a change in the conductivity of the outer shell by a factor of  $g_X^2$ . Choosing  $g_X$  to be somewhat less than unity then represents a way of effectively accounting for a lower metal conductivity in this outer shell layer due to electrons in this layer interacting with the surfactant and thus contributing less to conductivity. Regarding the present calculations, we take  $g_{\text{Ag}} = 0.85$ . This is slightly (6%) larger than in previous work on Ag nanoparticles<sup>2</sup> to account for the incomplete coverage of the surfactant molecules in the dimer systems. We take  $g_{\text{Au}} = 0.9$ , somewhat larger than the corresponding value for Ag, because we expect the surfactant layer to reduce the electron density of Au by a smaller margin compared to Ag. The electron affinity of Au is greater than that of Ag, so Au will tend to retain more electron density.<sup>3,4</sup> Furthermore, the gold surface is partially passivated by a thin iron oxide layer, so this will inhibit the adsorption of OAm on the gold surface to some extent.

The damping constant,  $\gamma_X$ , is interpreted classically as the inverse of the mean lifetime between electron scattering events; quantum mechanically,  $\gamma_X$  is related to broadening of the plasmon that results from dipolar transitions between discrete eigenstates with transition energies near the plasmon frequency.<sup>5-11</sup> In both interpretations, the damping is inversely proportional to the particle size, and both the particle size and the chemical nature of the particle/medium interface can have a profound impact on the damping. A frequently used phenomenological size correction for a spherical nanoparticle of radius  $a$  is given by

$$\gamma_X = \gamma_X^0 + \frac{3A_X v_X^F}{4a}, \quad (\text{S5})$$

where  $\gamma_X^0$  is the bulk metal damping constant,  $v_X^F$  is the Fermi velocity and  $A_X$  is a parameter (of order unity) which describes the damping contribution of the metal/medium interface.<sup>5-10</sup> To account for the effects of more than one type of surface interface, we have implemented a generalization of the size correction due to Liu and Sionnest.<sup>11</sup> Explicitly, for our interfaced Au-Ag heterodimers, the correction has the form

$$\begin{aligned}\gamma_{Ag} &= \gamma_{Ag}^0 + \frac{v_{Ag}^F}{4V_{eff}} \left( A_{Ag,s} S_{Ag,s} + A_{Ag,Au} S_{Ag,Au} \right) \\ \gamma_{Au} &= \gamma_{Au}^0 + \frac{v_{Au}^F}{4V_{eff}} \left( A_{Au,s} S_{Au,s} + A_{Au,Ag} S_{Au,Ag} \right)\end{aligned}, \quad (S6)$$

where  $V_{eff}$  is the volume of the composite particle,  $A_{X,Y}$  denotes a damping factor for interface  $X/Y$ , and  $S_{X,Y}$  is the surface area associated with the interface  $X/Y$ . The label “s” in Eq. (S6) denotes an interface with the surfactant layer. Note that  $A_{Au,Ag}$  is not required to equal  $A_{Ag,Au}$ . Values for the volume and various surface areas are determined from the geometry of the interfaced Au-Ag heterodimers shown in Figure S2. The spherical morphology and size of the Au nanoparticles and the Au/Ag intersection (highlighted by the black line in Figure S2A) in a heterodimer are assumed to remain unchanged during the growth of the Ag domain. Careful analysis of the TEM images and EDS spectra of products formed at different reaction times results in the detailed dimensional parameters of the heterodimers (Figure S2C).

The various  $A_{X,Y}$  factors in Eq. (S6) are obtained by fitting the DDA-based absorption cross sections to the experimental data in Figure 2. The value of  $A_{Au,s}$  is obtained by fitting to  $t = 0$  s result that corresponds to an isolated Au nanoparticle in hexane and a value of  $A_{Au,s} = 0.9$  is found. In the similar way,  $A_{Ag,s}$  can be obtained by fitting to the longer reaction time limit where the  $\sim 410$  nm spectral region is dominated by Ag, yielding  $A_{Ag,s} = 0.75$ . The final two parameters  $A_{Au,Ag}$  and  $A_{Ag,Au}$  are determined to best describe the nuances of the intermediate reaction times:  $A_{Au,Ag} = 0.125$  and  $A_{Ag,Au} = 1.0$ .

The relative values of all the various  $A_{X,Y}$  are physically reasonable. For example, the enhancement of PK2 at 2 s relative to 0 s (pure Au) indicates that the formation of a Au/Ag interface reduces the damping of Au’s electrons relative to the Au-surfactant interface. This means that  $A_{Au,Ag}$  should be smaller than  $A_{Au,s}$ . In contrast, no absorption peak corresponding to the Ag SPR is observed in the particles formed at 2s (red curve, Figure 2), indicating that formation of the Au/Ag interface increases the damping of Ag’s electrons and the corresponding  $A_{Ag,Au}$  should be larger than  $A_{Ag,s}$ . Finally, we deduce that  $A_{Ag,Au} > A_{Au,Ag}$ , which can be understood as follows. Although Au and Ag are in conductive contact and the interface is not a hard-wall boundary on the electron density, the presence of this interface does have an impact on the electronic eigenstates in the Au and Ag domain, and consequently contributes to damping of the various SPR modes. In general, we expect that damping of the SPR modes will be larger

when there is a greater density of unoccupied single-particle states near the Fermi energy ( $E_F$ )<sup>12</sup>. We have performed density functional theory (DFT) calculations on a prototype  $Ag_{14}Au_{10}$  cluster, which show a significant shift in electron density from the silver domain to the gold domain (see Figure S8). Consequently, the conductive contact between silver and gold will *increase* the density of unoccupied single-particle states close to the Fermi energy ( $E_F$ ) localized on the silver domain; conversely, the conductive contact between silver and gold will *decrease* the density of unoccupied single-particle states close to  $E_F$  localized on the gold domain. From these considerations, we infer that the interface between silver and gold will lead to larger damping of SPR modes in the silver domain than in the gold domain, hence  $A_{Ag,Au} > A_{Au,Ag}$ , which is consistent with the observed spectral behavior.

## B. Electrodynamics Computational Details

We simulate the absorption spectra of the interfaced Au-Ag heterodimers using the discrete dipole approximation (DDA) incorporating the code DDSCAT.<sup>13,14</sup> Because the experimental particles are randomly oriented in the solvent of hexane, our calculated spectra are orientationally averaged. Due to symmetry, only two rotational angles are sampled in the averaging. The reported spectra sample 15 orientations. Calibration calculations sampling as many as 143 orientations are also performed to verify that the sparser sampling used can yield accurate results. Each dimer is represented by an array of approximately 100,000 dipoles with polarizabilities encoded through frequency-dependent dielectric functions. The dielectric functions for the metal domains are corrected as described in the previous section (Section 2A) and in the manuscript main text. Calibrations are also performed for spherical gold and silver particles against the exact Mie theory results to test convergence of the absorption cross sections with respect to dipole number. It is noted that the convergence of the absorption cross section of silver is rather slow with the number of dipoles, however, the accuracy of the cross sections with 100,000 dipoles is adequate for our purposes. DDSCAT can be used to calculate the electric field at in a small volume enclosing the target particles, called the nearfield. We use this information directly and plot the near field electric field distributions in Figure 4.

## C. Electronic Structure Computational Details

The experimental spectra contain rich information that allows inference about the physics that

give rise to the relative magnitudes of the different interface prefactors  $A$ . Electronic structure calculations are performed on a prototype interfaced AuAg cluster to corroborate physical arguments behind our choice of values of  $A_{X,Y}$  for the silver-gold and gold-silver interfaces, as well as the relative magnitude of the factor  $g$  used to modify the electron density in the surface layers of the Au and Ag domains. The physical arguments behind these parameters are consistent with an increased localization of electron density on the gold domain and a decreased localization of electrons on the silver domain, leading to a commensurate increase in unoccupied single-particle states close to the Fermi energy and localized on the silver domain and a decrease in unoccupied single-particle states close to the Fermi energy localized on the gold domain. We calculate the ground-state electronic structure of a prototype  $\text{Au}_{10}\text{Ag}_{14}$  cluster using density functional theory (DFT) with the computational suite NWChem.<sup>15</sup> First, a  $\text{Ag}_{24}$  cluster was optimized at the PBE0/LANL2DZ level.<sup>16-19</sup> The starting coordinates for the  $\text{Ag}_{24}$  cluster correspond to a Sutton-Chen cluster with a 12-6 potential taken from the Cambridge Cluster Database,<sup>20</sup> scaled by the lattice constant of Ag (4.09 Å). Subsequently, 10 Ag atoms are substituted with Au atoms in the cluster to create a segregated Au domain (see Figure S6A). Optimizing the  $\text{Au}_{10}\text{Ag}_{14}$  geometry at the PBE0/LANL2DZ level leads to mixing of Au and Ag domains, but the optimized structure and the structure picture in Figure S6A show similar localization of the electron density on gold-dense regions compared to Ag-dense regions, hence the un-relaxed  $\text{Au}_{10}\text{Ag}_{14}$  (i.e., with segregated Au and Ag domains) ground-state electron density is presented in Figure S6B for ease of visualization. The ground state electronic structure was calculated at the same level of theory and the charge density was visualized using Molden<sup>21</sup> (Figure S6C).

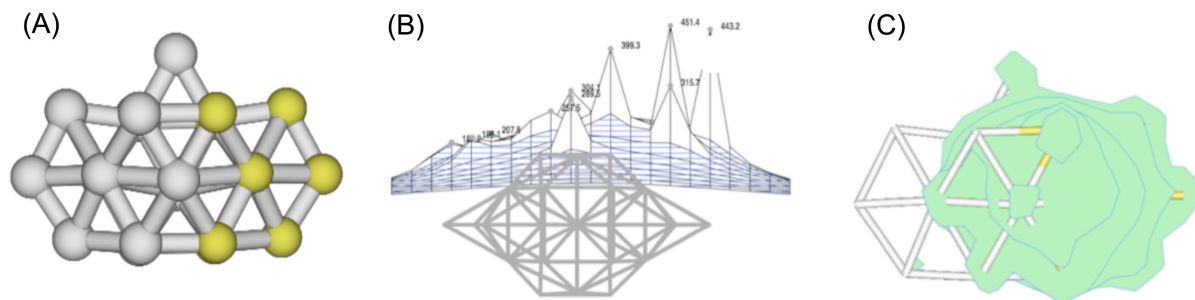


**Figure S6.** Structure of the prototype interfaced Au<sub>10</sub>Ag<sub>14</sub> cluster (A), charge density profile (B) and contour map (C) of the charge density of the cluster. The results show the increased localization of charge density on the gold domain and, to a lesser extent, at the silver-gold interface.

#### References:

1. Johnson, P. B.; Christy, R. W. *Phys. Rev. B* **1972**, *6*, 4370-4379.
2. Peng, S.; McMahon, J. M.; Schatz, G. C.; Gray, S. K.; Sun, Y. *Proceedings of the National Academy of Sciences* **2010**, *107*, (33), 14530-14534.
3. Bilodeau, R. C.; Scheer, M.; Haugen, H. K. *J. Phys. B: At. Mol. Opt. Phys.* **1998**, *31*, 3885-3891.
4. Andersen, T.; Haugen, H. K.; Hotop, H. *J. Phys. Chem. Ref. Data* **1999**, *28*, (6), 1511-1533.
5. Kawabata, A.; Kubo, R. *J. Phys. Soc. Japan.* **1966**, *21*, 1765-1772.
6. Baida, H.; Billaud, P.; Marhaba, S.; Christofilos, D.; Cottancin, E.; Crut, A.; Lermé, J.; Maili, P.; Pellarin, M.; Broyer, M.; Del Fatti, N.; Vallée, F.; Sánchez-Iglesias, A.; Pastoriza-Santos, I.; Liz-Marzán, L. M. *Nano. Lett.* **2009**, *9*, 3463-3469.
7. Lermé, J.; Baida, H.; Bonnet, C.; Broyer, M.; Cottancin, E.; Crut, A.; Maioli, P.; Del Fatti, N.; Vallée, F.; Pellarin, M.; *J. Phys. Chem. Lett.* **2010**, *1*, 2922-2928.
8. Genzel, L.; Martin, T. P.; Kreibig, U. *Z. Physik. B* **1975**, *21*, 339-346.
9. Kraus, W. A.; Schatz, G. C. *J. Chem. Phys.* **1983**, *79*, 6130-6139.
10. Coronado, E. A.; Schatz, G. C. *J. Chem. Phys.* **2003**, *119*, 3926-3924.
11. Liu, M.; Guyot-Sionnest, P. *The Journal of Physical Chemistry B* **2004**, *108*, (19), 5882-5888.

12. Ibach, H.; Lüth, H., *Solid-State Physics: An introduction to principles of materials science*. Fourth Edition ed.; Springer-Verlag: 2009.
13. Draine, B. T.; Flatau, P. J. *J. Opt. Soc. Am. A* **1994**, 11, (4), 1491-1499.
14. Flatau, P. J.; Draine, B. T. *Opt. Exp.* **2012**, 20, (2), 1247-1252.
15. Valiev, M.; Bylaska, E. J.; Govind, N.; Kowalski, K.; Straatsma, T. P.; Van Dam, H. J. J.; Wang, D.; Nieplocha, J.; Apra, E.; Windus, T. L.; de Jong, W. A. *Comput. Phys. Commun.* **2010**, 181, 1477-1489.
16. Adamo, C.; Barone, V. *J. Chem. Phys.* **1999**, 110, (13), 6158-6170.
17. Perdew, J. P.; Burke, K.; Ernzerhof, M. *Phys. Rev. Lett.* **1996**, 77, (18), 3865-3868.
18. Hay, P. J.; Wadt, W. R. *J. Chem. Phys.* **1985**, 82, (1), 299-310.
19. Hay, P. J.; Wadt, W. R. *J. Chem. Phys.* **1985**, 82, (1), 270-283.
20. Wales, D. J.; Doye, J. P. K.; Dullweber, A.; Hodges, M. P.; Naumkin, F. Y.; Calvo, F.; Hernández-Rojas, J.; Middleton, T. F., The Cambridge Cluster Database. In <http://www-wales.ch.cam.ac.uk/CCD.html>.
21. Schaftenaar, G.; Noordik, J. H. *J. Comput. Aided Mol. Design* **2000**, 14, 123-134.